Microchemical Journal 103 (2012) 148–157

Contents lists available at SciVerse ScienceDirect

Microchemical Journal

journal homepage: www.elsevier.com/locate/microc

Microchemistry and stable isotope systematics of gold mineralization in a gabbro–diorite complex, SE Egypt

Basem Ahmed Zoheir

Department of Geology, Faculty of Science, Benha University, 13518, Egypt

ARTICLE INFO

Article history:
Received 5 February 2012
Received in revised form 12 February 2012
Accepted 12 February 2012
Available online 16 February 2012

Keywords:
Microchemistry
Stable isotopes
Um Eleiga gold deposit
Island arc intrusive complex
Egypt

ABSTRACT

Electron probe micro-analysis (EPMA) and laser ablation-inductively coupled plasma-mass spectrometry (LA-ICP-MS) data of ore minerals from the Um Eleiga deposit (SE Egypt) suggest that primary Au was sequestered within Ni–pyrrhotite and Co–Ni–Fe sulfarsenide, while refined, free-milling gold grains (~93 wt.% Au) are associated with late pyrite, or occur along micro-fractures in quartz veins. A magmatic source of gold is most likely, yet endowment by circulating metasomatic fluid was crucial for Au concentration.
Sulfur stable isotope values ($\delta^{34}S$) of sulfide minerals disseminated in the quartz veins (pyrite: −0.5 to 1.5‰, chalcopyrite: −0.3 to 0.6‰, and sphalerite: −0.1 to −0.4‰), indicate a generally light sulfur source. Similarly, measured $\delta^{13}C$ of vein calcite (−3.1 to −1.8, n = 9) and calculated fluid $\delta^{13}C_{CO2}$ values (−0.6 to 0.6‰, for the temperature range 350–375 °C of associated hydrothermal chlorite) cluster around 0‰, consistent with a magmatic source for carbon. Oxygen isotope data for vein calcite (10.3–13‰, n = 9) and quartz (11.7–14.3‰, n = 10) indicate average fluid $\delta^{18}O_{H2O}$ values of 7.4 and 7.8‰, respectively, which implicate fluids similar to those in intrusion-related systems.

1. Introduction

Egypt is a typical example of a country where historical gold was recovered from lodes and placer deposits. A large number of different primary and secondary gold deposits are known within the Precambrian basement and cover rocks in the Eastern Desert. Previous workers [1–6] suggest genetic relationships between these deposits and plutonic/metamorphic terranes, structural elements or tectonic events, but rarely take into account the implication of the mineralization style and ore microchemistry.

Two broad occurrences of gold ores are defined by their ease of determination with various techniques. The most common is known as visible gold that is identifiable by conventional microscopy. This occurrence of gold comprises all free-milling gold and the majority of refractory gold. The other occurrence is the more controversially named 'invisible' gold, often described as sub-micron or molecular gold, which occurs as colloidal particles or in solid solution within a mineral matrix. Microchemical characterization of the gold-sulfide ores by electron microprobe and LA-ICP MS analyses has been shown to be an effective tool to distinguish different types of mineralization, to detect zonation within a mineralized area and discriminate between gold of primary and secondary origins [e.g., 7–9]. Linkage of various styles of source mineralization with particular geological environments aids a more effective gold exploration targeting and reevaluation plans of well-established alluvial goldfields [10].

Chemically, gold behaves as a siderophile and chalcophile element, consistent with its association with sulfide minerals in most magmatic and hydrothermal systems [11,12]. Experimental investigations indicate that gold is strongly partitioned into sulfide minerals precipitating from felsic silicate melts [e.g., 13–15]. Natural systems appear to show the same behavior, suggesting that gold distribution in igneous systems is controlled by sulfide minerals [16, references therein]. Granitoid intrusions may provide heat necessary to initiate and maintain hydrothermal systems, and can provide some of the metals for associated ore deposits [13,17]. During magmatic–hydrothermal evolution, Au partitions into exsolved magmatic fluids, under suitable physiochemical conditions and geological environment. Consequently, a gold deposit originating from magmatic fluids may form within the intrusion or peripheral country rocks [18].

This work builds on preliminary petrologic and geochemical studies of the Um Eleiga complex [19] to reveal the relationship between gold mineralization and the host intrusive complex. New microprobe and laser ablation inductively coupled plasma data of the ore minerals together with stable isotope systematic have been used to define the metal and fluid sources as an important implication for gold genesis and assessment of old and new targets.

2. Geologic setting

Progressive cratonization by development of numerous magmatic arcs and closure of back arc basins to assemble a continental shield is

E-mail address: basem.zoheir@gmail.com.

0026-265X/$ – see front matter © 2012 Elsevier B.V. All rights reserved.
doi:10.1016/j.microc.2012.02.003

proposed as the tectonic evolution of the Arabian Nubian Shield (900–550 Ma) [20–22]. Gabbro–diorite (±tonalite±granodiorite) suite, together with calc-alkaline volcanic and volcaniclastic sequences, generally metamorphosed under greenschist facies conditions, represents the early manifestations of the island–arc activity in the Arabian–Nubian Shield [23,24]. Rb–Sr whole-rock dating of the gabbro–diorite complexes spreading over the Eastern Desert of Egypt indicates early Pan-African ages (881±58 Ma) [25,26]. These complexes include calc-alkaline granitoid rocks showing petrological characteristics of the M-type granites, and are likely related to magmas generated from a mantle wedge above an early Pan-African subduction zone, subsequently fractionated to give the more felsic varieties [23].

The Um Eleiga intrusive complex (ca. 32 km^2) is located at ~45 km due west of the Red Sea coast in the South Eastern Desert of Egypt (Fig. 1). Although dominated by gabbro and diorite, the complex encompasses a compositional continuum from quartz gabbro to granodiorite, through diorite and tonalite. Zoheir et al. [19] describe a concentric and reversed zoning pattern, in which the felsic rocks dip inward beneath the intermediate/mafic core. Formation of this intrusive complex is attributed to subducted slab components that interacted with and contaminated by upper mantle wedge under conditions of 3–5 kbar and ~720 to 880 °C [19].

The Um Eleiga complex cuts the allochthonous ophiolitic serpentinite–chromitite massif (Gebel Abu Dahr), and a highly tectonized matrix of metavolcanic–metasedimentary sequences [27]. Abundant xenoliths and roof-pendants of chromite-bearing mafic/ultramafic rocks are observed in all parts of the complex. Non-pervasive foliation, marked by alternate feldspar-rich and hornblende-rich bands, is best developed in the marginal parts of the complex. Contacts between the different rock varieties in the complex are gradational, and no crosscutting relationships have been observed. In places, the gabbroic and granitoid units merge into each other along zones densely dissected by fault/fracture sets, commonly in WNW–ESE, NNW–SSE and N–S directions. The gabbroic rocks are variably olivine-, pyroxene- and/or hornblende-rich, and are locally highly strained. Diorite surrounds the gabbroic core and constitutes the largest voluminous portion of the complex. Locally, diorite exhibits a distinct porphyritic texture, in which patchy feldspar crystals (≤0.7 mm across) are embedded in a hornblende-rich groundmass. Tonalite and granodiorite constitute the peripheral parts of the complex. Flat-lying dyke like bodies of highly albitized granite cut diorite, whereas, irregular bodies of syn-orogenic microdiorite and fine-grained granodiorite cut the western part of the complex. Abundant lamprophyre and andesite dykes as well as microgranite dykes are observed in all parts of the complex.

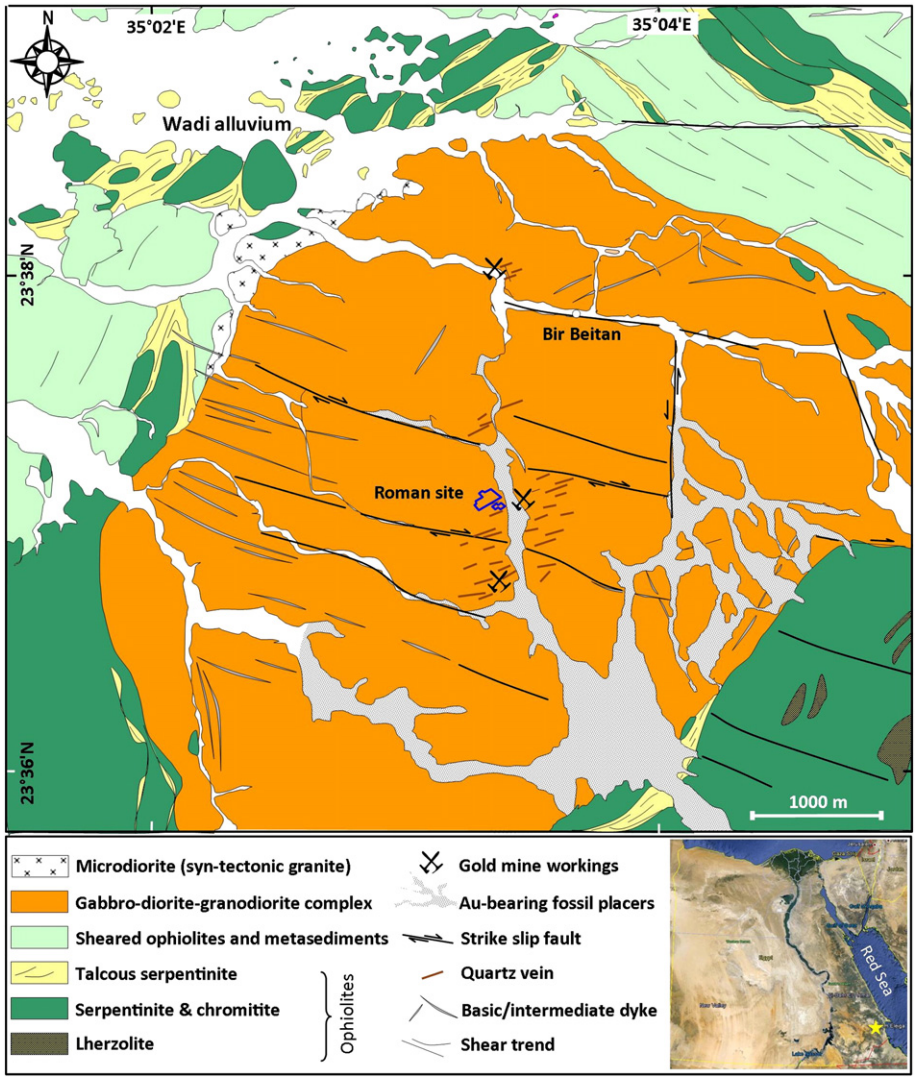

Fig. 1. Geological map of the Um Eleiga gold deposit.
Modified from Hassan and El-Manakhly [29] and Zoheir et al. [19].

3. Gold mineralization

The Um Eleiga area is known for a historic gold mine that was active during the Roman–Byzantine and early Islamic eras [28]. The bulk gold mineralization in the area is related to sulfide-bearing quartz veins that have severally eroded and dispersed everywhere in the drainage network. Elevated gold values have been reported in samples collected from the central part of the area, along the N–S trending Wadi Um Eleiga and along small WNW-trending tributaries. Analyses of quartz dumps in more than a hundred pits revealed up to 28 mg/kg Au [29]. Exposures of gold-bearing quartz veins are uncommon, and no subsurface mine workings have been observed. Instead, most of the ancient mining is confined to the terraces (~2.5 km^2), where several tributaries merge into a wide single confluence (Fig. 1). Hundreds of open pits, trenches, stone anvils, hammers, and grinding wheels may indicate that reworked fragments of the auriferous quartz were the prime mining targets. The stopped out terraces are mainly lithified alluvium of ill-sorted, fragments of quartz, gabbroic and ultrabasic rocks cemented by brownish earthy material. Atomic absorption analyses of heavy concentrates of the Wadi alluvium (terraces) give gold values from traces to 36 mg/kg [3, references therein]. Dumps of gold-bearing milky quartz veins with slivers of chlorite–sericite–carbonate materials have been observed where pyrite, malachite, limonite and chalcedonic quartz are abundant. In a few cases, the open pits expose mineralized quartz lodes. The quartz veins are mostly narrow (5 to 40 cm thick) with brecciated borders, where quartz fragments are cemented by mixtures of chalcedonic quartz, chlorite and sulfides (Fig. 2A). Inspection of the internal structure of these veins reveals dominant coarse-grained, comb quartz and calcite and subordinate chlorite, sulfide and fine-grained quartz (Fig. 2B). Quartz subgrains intermingle with calcite and chlorite along fractures or along the boundaries of large quartz grains (Fig. 2C). Large idiomorphic vein quartz crystals enclose or intermingle with calcite, and locally exhibit growth-bound trails of fluid inclusions (Fig. 2D).

Lenticular bodies of quartz (±calcite) cut gabbroic and diorite rocks, commonly next to the large faults/fracture zones. These bodies contain slivers of altered wallrock rich in chlorite, sericite and disseminated sulfides. On the other hand, stockwork of milky quartz lack disseminated sulfides are confined to zones of highly bercciated gabbroic rocks. They are considered tension gashes, generally characterized by drusy structures. Zoheir et al. [19] suggest that zones of intense hydrothermal alteration and related high gold grades in the central part of the Um Eleiga complex are controlled by fault/joint intersections. The altered gabbroic rocks contain disseminated gold grains commonly along microfractures, particularly close to hydrothermal chlorite. Ore minerals disseminated in the quartz veins and adjacent wallrocks are mainly pyrite, chalcopyrite, and minor amounts of sphalerite, Ni–Fe–Co–sulfarsenide (Fe–Ni–cobaltite?), pyrrhotite, and gold. Intergrowth and replacement textures suggest that pyrrhotite and sulfarsenide are early phases, while pyrite, chalcopyrite, sphalerite and free gold are late in paragenesis.

The hydrothermal alteration assemblage in host rocks associated with the gold-sulfide mineralization comprises variable proportions of quartz, chlorite, calcite, sericite, rutile and sulfide minerals. This assemblage clearly overprints the igneous paragenesis of the host rocks

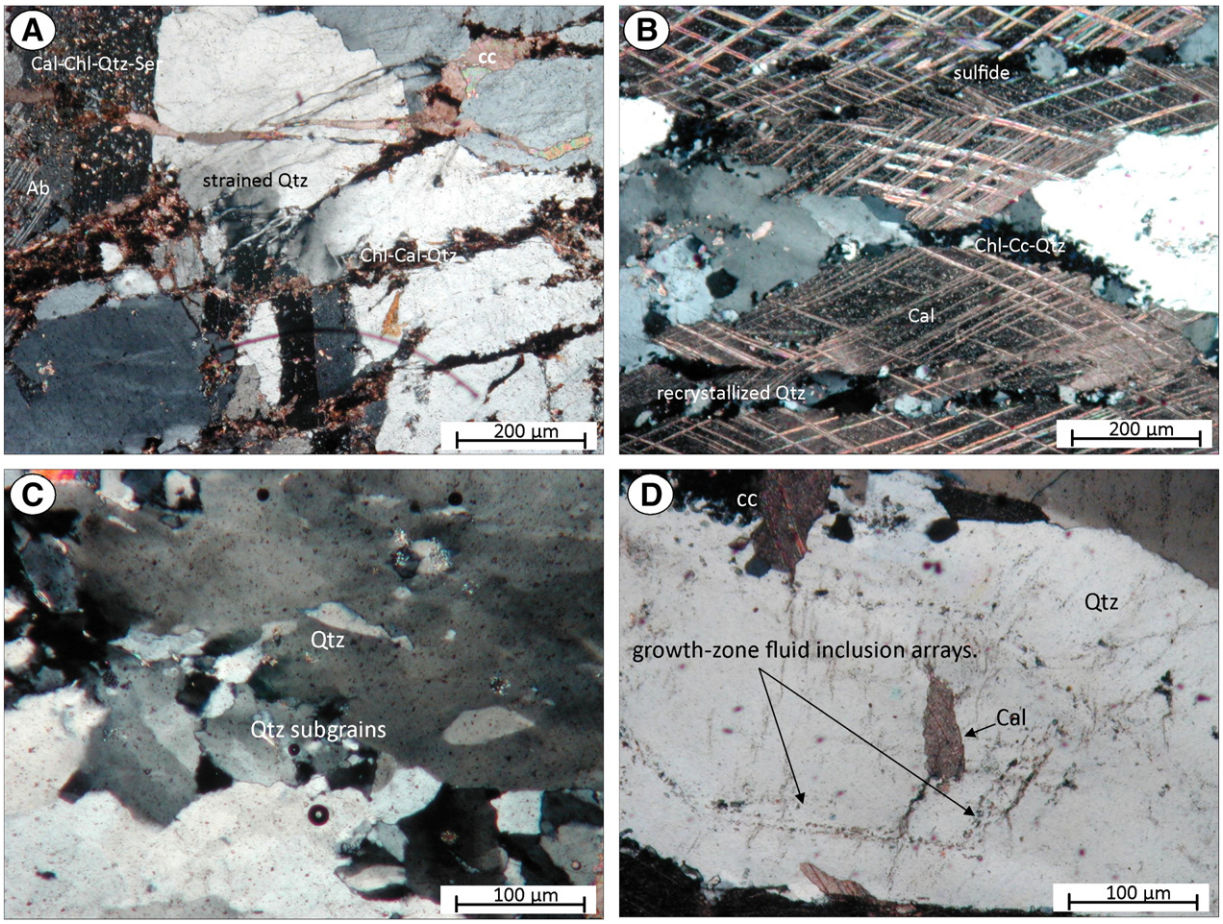

Fig. 2. Photomicrographs of mineralized quartz veins showing: (A) Fragmented vein quartz and albite (Ab) sealed by calcite (Cal), chlorite (Chl), sericite (Ser) subordinate sulfides and fine-grained quartz (Qtz), (B) Calcite-dominated vein with ribbon and recrystallized quartz intermingles with fine-grained Fe-rich chlorite, (C) Recrystallization and subgrain development along boundaries of large quartz crystals in vein quartz, (D) Idiomorphic vein-quartz crystal containing primary growth-zone fluid inclusions.

and shows a disseminated, non-oriented pattern (Figs. 3A–C). Disseminated sulfides are commonly associated with pervasive quartz–sericite–chlorite alteration (Figs. 3A, B). Iron-stain is common along E-trending fractures within the chlorite–calcite-rich domains in the altered gabbroic rocks. Comb and chalcedonic quartz fill the microfractures and seal crushed quartz fragments or form thin veinlets (0.2 to 3 cm-thick) commonly in the highly fractured host rocks. Partial or complete replacement of pyrite and chalcopyrite by goethite and malachite and azurite is ubiquitous (Fig. 3D).

4. Methods

SEM back-scattered electron imaging and quantitative electron microprobe analyses of major and minor elements in hydrothermal ore and gangue minerals were obtained on a Cameca SX100 four spectrometer, fully automated electron microprobe at the TU Clausthal (Germany). Analyses of sulfide minerals were carried out under conditions of 20 keV accelerating voltage and 40 nA beam current and counting times of 10 to 60 s, using a 2 μm beam diameter. Natural and synthetic sulfides were used as reference materials. The analyses were corrected for electron beam-matrix effects, and instrumental drift and dead time using a Phi-Rho-Z (CITZAF) [30] scheme as supplied with the Cameca SX100 electron microprobe. Relative accuracy of the analyses, based upon comparison between measured and published compositions of standard reference materials, is ~1–2% for concentrations >1 wt.% and ~5–10% for concentrations <1 wt.%. Carbonate minerals, sericite and chlorite disseminated in quartz veins and mineralized wallrocks have been analyzed under operating conditions of 15 kV, 20 nA beam current and a 5 μm beam diameter.

Gold contents in sulfide and sulfarsenide phases were determined by LA-ICP-MS. Gold analysis was conducted using an Agilent 7500i Quadrupole ICP-MS instrument, coupled with a New Wave (Merchantek) LUV266x LA system at the University of Erlangen (Germany). The laser beam was fired at 10 Hz repetition rate with the laser energy in the range of 0.36–0.51 mJ per pulse. A spot size of 30 μm was used, which represented the optimum value for a good spatial resolution at the desired level of analytical precision and detection limit. All data were collected in time-resolved mode; 20 s instrumental background measurement (carrier gas + LA-ICP MS) followed by 20 s sample ablation. Data reduction and calculation of concentrations were performed with the GLITTER 3.0 software package [31]. Analytical errors were calculated as 1σ, and the minimum detection limit at the 99% confidence level was determined by Poisson counting statistics. Calibration for a quantitative determination of gold was done using a certified external reference material, i.e. the synthetic pyrrhotite PO-724-B3 obtained from Memorial University of Newfoundland, Canada (with 47.3 mg/kg Au). Both the external reference material and the samples were analyzed under conditions identical to those detailed above. Reproducibility of the analytical results was controlled by means of replicate measurements of the external

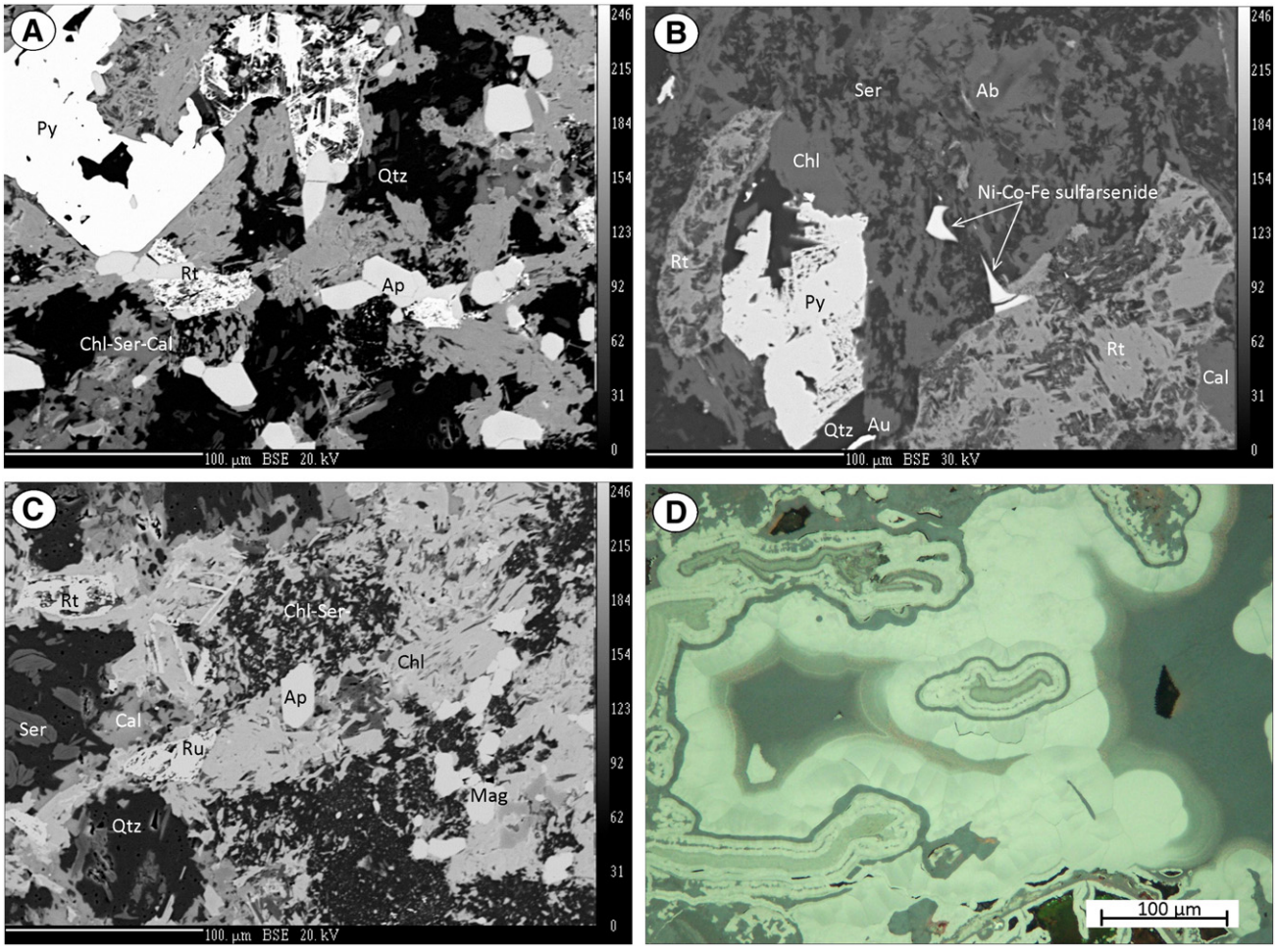

Fig. 3. (A) SEM backscattered electron image of altered, mineralized gabbroic sliver in quartz vein showing disseminated pyrite (Py) associated with chlorite (Chl), sericite (Ser), calcite (Cal) and abundant apatite (Ap). Rutile (Rt) overprints the sulfide mineralization, (B) SEM backscattered electron image of altered, mineralized diorite wallrock with disseminated pyrite, sulfarsenide, rutile and gold (Au) associated with hydrothermal quartz, chlorite, sericite and calcite, (C) SEM backscattered electron image of altered wallrock with abundant disseminated sericite–calcite–chlorite–quartz and magnetite (Mag), (D) Reflected-light photomicrograph of highly oxidized wallrock showing botryoidal malachite and azurite replace copper sulfides.

standard. For the given analytical conditions, the 1σ error is in the range of 5%–10% above absolute Au concentrations of 1 mg/kg.

5. Microprobe data of the hydrothermal gangue and ore minerals

5.1. Gangue minerals

Hydrothermal chlorite, calcite and less abundant sericite intermingle with vein quartz or disseminated in slivers of the wallrock (see Figs. 2, 3). Chlorite flakes in the altered wallrocks are associated with fine-grained quartz and disseminated pyrite and chalcopyrite. Electron probe data of chlorite flakes in lodes and wallrocks have generally Fe-rich composition (FeO^t 19.8–27.7 wt.%; Table 1). Calculated structural formula on 14 oxygens indicate identical values of Si (2.64–2.72 apfu), Al^{iv} (1.28–1.34 apfu), and Mg (1.66–2.51 apfu). Fe/(Fe + Mg) ratios are mostly identical (0.41–0.60). The formation temperature of chlorite was calculated using the empirical Si–Al^{iv} substitution geothermometer of Cathelineau [32] and Jowett [33]. A consistent, narrow range of temperatures (350–375 °C) is estimated. The calculated absolute temperatures using these two thermometers are identical in most cases (Table 1).

Sericite disseminated in the mineralized quartz veins and wallrocks is associated with chlorite and calcite. Electron microprobe data of the sericite disseminated in the veins and wallrocks are identical (Table 1). Representative chemical compositions of the investigated flakes show relatively high FeO^t contents (2.01–3.76 wt.%), MgO (0.12–0.45 wt.%) and Na_2O (0.26–0.75 wt.%). Muscovite component is high in all analyzed flakes (X_{Ms} = 0.94–0.96). The phengite content (Mg + Fe a.p.f.u.) varies from 0.13 to 0.25, with no systematic decrease noticed in vein and wallrock sericites.

Calcite is disseminated in the quartz veins and wallrocks or occurs as thin veinlets close to the mineralized quartz veins. Calcite has a nearly stoichiometric composition with small amounts of MgO (up to 1.16 wt.%), FeO (up to 0.65 wt.%), MnO (up to 0.58 wt.%). Calculated on basis of 6 oxygens and 2 cations, the analyzed calcite grains show a nearly pure calcite component (up to 98 mol% $CaCO_3$), and minor components of $CaMg(CO_3)_2$ (up to 4.76 mol%), up to 2.66 mol% $CaFe(CO_3)_2$, and up to 2.26 mol% $CaMn(CO_3)_2$ (Table 1).

5.2. Ore minerals

Pyrite occurs as disseminated subhedral or anhedral grains, in isolation or clustered into patchy aggregates (Figs. 4A–D). Data of the analyzed pyrite grain reveal a stoichiometric composition (Table 2), with no detectable concentrations of minor elements (e.g., Ni, Co, Cd, Sb…etc.). Inclusions of pyrrhotite are common in the large pyrite grains. Pyrrhotite is Ni-bearing, with compositions formulated as $Fe_{0.93}Ni_{0.02}S_{1.05}$ (Table 2). Dispersed specks of Fe–Co–Ni–sulfarsenides, commonly associated with pyrrhotite, are disseminated in quartz, commonly adsorbed on pyrite grains (Figs. 4C–D). These phases have a generally (Ni,Sb)-poor, Fe-cobaltite composition with As/S values greater than 1.5. The calculated structural formulas of the analyzed grains (average $Ni_{0.1}Fe_{0.3}Co_{0.6}As_{0.86}S_{1.1}$) showed that Fe forms ~0.3 atoms per formula unit (apfu), indicating significantly lower formation temperatures [e.g., 34,35].

Chalcopyrite and sphalerite occur either intergrown with small subhedral pyrite grains or as small inclusions in fractured grains associated with gold blebs (Figs. 4A–D). Electron microprobe results on chalcopyrite and sphalerite showed that they are close to stoichiometric in composition. Chalcopyrite contains only some traces of Zn (up to 0.25 wt.%). It has an average structural formula of $Cu_{0.94}Fe_{1.09}S_{1.97}$. Sphalerite composition is uniform ($Fe_{0.1}Zn_{0.9}S_1$), with Fe contents of ~4 to 7 wt.%, and Cu from 0.71 to 2.21 wt.%, while all other elements are below the detection limit (Table 2).

Visible gold is observed in a few cases. Microscopic and submicroscopic free-milling gold grains occur as dispersed blebs and specks along fine ribbons of wallrock in the quartz veins. Dispersed inclusions of gold (a few μm-across) have been observed in pyrite, associated with Ni–Fe–Co–sulfarsenide, or occur along microfractures (Figs. 4B–D). Gold grain compositions are mainly high fineness electrum (~935) with no traces of Te and Sb (Table 2).

5.3. Gold abundance by LA-ICP MS

The average S content in each sulfide grain was used as an internal standard in (LA-ICP MS) analysis of that grain. Substantial contents of dissolved gold were reported in Ni-bearing pyrrhotite and in Ni–Fe–Co–sulfarsenide, whereas pyrite, chalcopyrite and sphalerite show no detectable Au (detection limit is calculated as 0.02 mg/kg). Pyrrhotite appears to contain significant gold values (up to 32 mg/kg), consistent with the capacity of pyrrhotite to host more gold at magmatic temperatures, ~700 °C [15,36]. A few grains of the Ni–Fe–Co–sulfarsenide, large enough for LA-ICP MS analysis, show gold contents up to 26 mg/kg, with a median value of 19 mg/kg (Fig. 5).

6. Stable isotopes

6.1. Sampling and analytical procedures

Quartz and calcite separates for oxygen and carbon isotope measurements, and sulfide minerals for sulfur analysis were separated from, lightly crushed (40–60 mesh), lode samples, then washed and hand-picked under a binocular microscope. All mineral separates were estimated to be ≥95% pure. Vein quartz separates were hand-picked, dried, and crushed to less than 0.2 mm, then cleaned in a 3:1 mix of concentrated hydrochloric and nitric acid on a hotplate at approximately 100 °C for 2 h. Quartz separates were then rinsed with deionized water ten times, rinsed twice with technical grade acetone to ensure all water was removed, and dried on a hotplate. The samples were then loaded to the mass spectrometer for measurement. Oxygen isotope ratios are reported relative to VSMOW (Vienna Standard Mean Ocean Water), and carbon isotope ratios are reported relative to PDB (Pee Dee Belemnite). Pure calcite separates were prepared for carbon and oxygen isotope analyses. Carbonate gas extractions were carried out following the standard procedure of McCrea [37]. The reaction time for calcite is 4 h using a thermostated water bath at 25 °C [37]. A Finnigan MAT 251 dual-inlet, multiple-collector, magnetic-sector, gas mass spectrometer was used to analyze the carbon and oxygen isotopes in the stable isotopic laboratory at the USGS.

Sulfide separates were dissolved using 14.0 N ultrapure HNO_3 and then dried and transformed into chloride using 12.0 N ultrapure HCl. Sulfur isotope analyses were carried out using 200-mesh pyrite, chalcopyrite and sphalerite pure samples. They were combusted with CuO in an oven at 1000 °C and in vacuum condition. Liberated SO_2 was frozen in a liquid nitrogen trap and after cryogenic separation from other gases the isotopic compositions were determined on a Finnigan MAT 252 mass spectrometer at the Stable Isotope and ICP/MS laboratory of the Lausanne University, Switzerland.

All data are reported in the delta (δ) notation, relative to Vienna Pee Dee Belemnite V-PDB (C), Vienna Standard Mean Ocean Water V-SMOW (O) and Vienna-Canyon Diablo troilite V-CDT (S). The quartz and calcite stable isotope results have a 2σ error of 0.2‰, while the analytical uncertainty for $\delta^{34}S$ is 0.5‰. Repeated analyses conducted on several samples confirmed the reproducibility of the results.

6.2. Results

Isotope values of the investigated sulfide minerals are given in Table 3. The $\delta^{34}S$ values of pyrite in quartz veins range from 1.5 to 0.5‰, with a mean value of 1.0‰. Chalcopyrite has $\delta^{34}S$ values of

Table 1
Representative electron microprobe data of hydrothermal gangue minerals associated with the Um Eleiga gold deposit.

Chlorite							
SiO_2	25.44	26.01	25.03	26.93	26.49	27.04	24.70
TiO_2	0.04	0.05	0.45	0.02	0.02	0.03	0.06
Al_2O_3	22.86	24.76	22.66	24.31	22.86	24.32	22.63
FeO	23.75	20.46	27.72	21.21	24.12	19.80	27.35
MnO	0.09	0.10	0.15	0.08	0.09	0.12	0.09
MgO	14.24	16.31	10.30	16.04	15.09	16.78	11.74
CaO	0.02	0.24	0.07	0.08	0.05	0.59	0.12
Cr_2O_3	0.02	0.01	0.03	0.00	0.00	0.00	0.03
Na_2O	0.02	0.00	0.07	0.00	0.01	0.04	0.03
K_2O	0.01	0.03	0.24	0.00	0.02	0.01	0.00
Total	86.49	88.01	86.70	88.68	88.75	88.75	86.80
Structural formula unit based on 14 oxygen							
Si	2.69	2.64	2.70	2.72	2.72	2.71	2.66
Ti	0.00	0.00	0.04	0.00	0.00	0.00	0.00
$Al^{(iv)}$	1.31	1.36	1.30	1.28	1.28	1.29	1.34
$Al^{(vi)}$	1.53	1.61	1.58	1.61	1.49	1.59	1.52
Al	2.84	2.97	2.88	2.89	2.77	2.88	2.87
$Fe^{(ii)}$	2.10	1.74	2.50	1.79	2.07	1.66	2.46
Mn	0.01	0.01	0.01	0.01	0.01	0.01	0.01
Mg	2.24	2.47	1.66	2.41	2.31	2.51	1.88
Ca	0.00	0.03	0.01	0.01	0.01	0.06	0.01
Cr	0.00	0.00	0.00	0.00	0.00	0.00	0.00
Na	0.00	0.00	0.01	0.00	0.00	0.01	0.01
K	0.00	0.00	0.03	0.00	0.00	0.00	0.00
Total	9.89	9.87	9.85	9.83	9.89	9.85	9.91
X_{Fe}	0.48	0.41	0.60	0.43	0.47	0.40	0.57
T*	361	375	357	351	350	352	371
T**	366	377	365	353	354	354	378

Sericite						
SiO_2	47.22	47.63	46.95	46.42	47.11	46.85
TiO_2	0.08	0.09	0.11	0.07	0.09	0.04
Al_2O_3	33.48	35.02	33.17	31.46	31.21	32.61
FeO	2.19	2.01	2.73	2.29	3.76	2.78
MnO	0.00	0.00	0.01	0.04	0.01	0.02
MgO	0.12	0.28	0.34	0.45	0.43	0.42
CaO	0.02	0.08	0.00	0.03	0.00	0.04
Cr_2O_3	0.06	0.00	0.03	0.00	0.00	0.07
Na_2O	0.34	0.37	0.75	0.48	0.29	0.26
K_2O	11.22	9.26	10.32	11.03	11.53	10.82
Total	94.74	94.75	94.41	92.27	94.44	93.92
Structural formula unit based on 11 oxygen						
Si	3.18	3.16	3.17	3.22	3.22	3.19
Ti	0.00	0.00	0.01	0.00	0.00	0.00
$Al^{(iv)}$	0.82	0.84	0.83	0.78	0.78	0.81
$Al^{(vi)}$	1.84	1.90	1.81	1.79	1.73	1.80
Al	2.66	2.74	2.64	2.57	2.51	2.61
$Fe^{(ii)}$	0.12	0.11	0.15	0.13	0.21	0.16
Mn	–	–	–	–	–	–
Mg	0.01	0.03	0.03	0.05	0.04	0.04
Ca	–	0.01	–	–	–	–
Cr	–	–	–	–	–	–
Na	0.04	0.05	0.10	0.06	0.04	0.03
K	0.96	0.78	0.89	0.98	1.00	0.94
Total	6.99	6.88	7.00	7.01	7.04	6.99
X_{Fe}	0.91	0.80	0.82	0.74	0.83	0.79
X_{Ms}	0.96	0.94	0.90	0.94	0.96	0.96

Calcite						
CaO	47.06	47.35	48.08	48.11	47.26	49.02
MgO	1.16	0.95	0.84	0.02	0.86	1.10
FeO	0.43	0.30	0.31	0.47	0.65	0.51
MnO	0.27	0.17	0.04	–	0.18	0.58
Sum	48.92	48.77	49.27	48.6	48.95	51.21
Structural formulae based on 6 oxygens, 2 cations						
Ca	1.92	1.94	1.95	1.98	1.93	1.91
Mg	0.05	0.04	0.03	–	0.04	0.04
Fe	0.02	0.01	0.01	0.02	0.03	0.02
Mn	0.01	0.01	–	–	0.01	0.02
Sum	2.00	2.00	2.00	2.00	2.00	2.00
End members						
$CaCO_3$	92.38	94.14	95.19	97.90	93.06	91.00
$CaMg(CO_3)_2$	4.76	3.90	3.41	0.06	3.53	4.27
$CaFe(CO_3)_2$	1.76	1.23	1.25	1.95	2.66	2.17
$CaMn(CO_3)_2$	1.10	0.69	0.15	–	0.74	2.26
Sum	100	100	100	100	100	100

Calculated chlorite temperatures in °C, T* Cathelineau [32], T** Jowett [33].

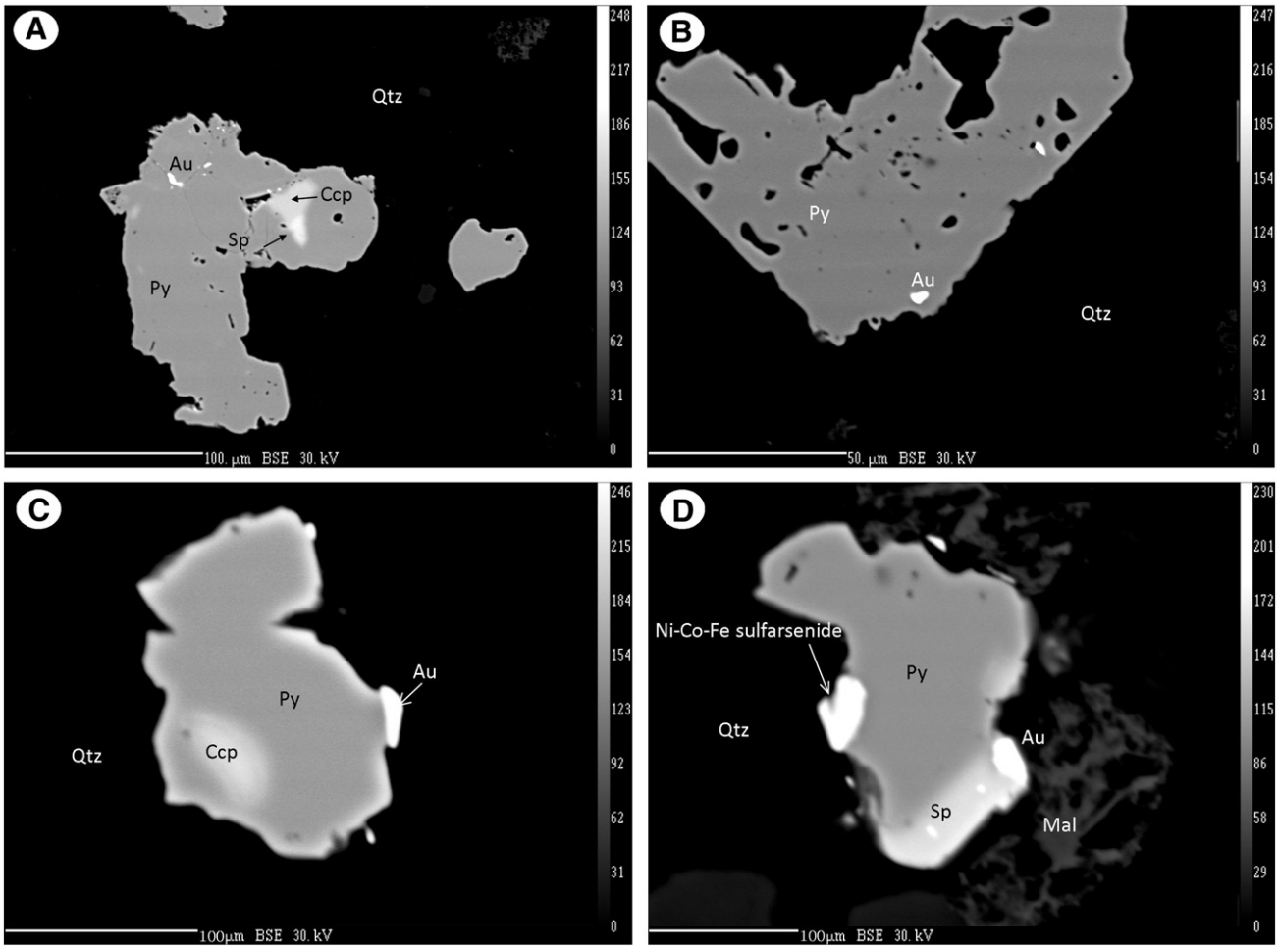

Fig. 4. (A) SEM backscattered electron image of disseminated ore minerals in quartz lodes. (A) Chalcopyrite (Ccp), sphalerite (Sp) and gold inclusions (Au) in anhedral pyrite (Py), (B) Fine gold inclusions are commonly near peripheries of the host pyrite grain, (C) Gold speck adsorbed to an anhedral pyrite intergrown with chalcopyrite (Ccp), (D) Ni–Co–Fe sulfarsenide and gold grains adsorbed to an anhedral pyrite grain that intergrown with sphalerite (Sp). The gray network in the host quartz vein is malachite (Mal).

Table 2
Representative electron microprobe data of sulfide and gold grains disseminated in quartz lodes from Um Eleiga gold deposit.

Pyrite										Chalcopyrite							
Fe	46.16	46.12	46.22	46.21	46.12	46.24	45.98	46.00	46.94	Fe	33.80	33.13	34.11	35.14	31.74	31.43	31.78
S	53.52	53.49	53.71	53.63	53.53	53.64	53.54	53.49	53.18	S	36.35	34.80	33.87	33.85	33.29	33.88	33.20
As	–	–	–	–	–	–	–	–	–	Ni	–	–	–	0.01	–	0.28	0.06
Co	–	–	–	–	–	–	–	–	–	Cu	28.27	31.92	31.78	30.64	34.12	34.43	34.18
Ni	–	0.05	–	–	–	–	0.08	0.06	0.03	Zn	0.25	0.14	0.00	0.00	0.11	0.23	0.00
Ag	–	0.01	0.01	0.01	–	–	–	0.07	–	Au	–	–	–	–	–	–	–
Au	0.01	0.02	0.02	–	0.02	0.04	0.02	0.02	–	Sb	–	–	–	–	–	–	–
Sb	–	–	–	–	–	–	–	–	–	Sum	98.81	99.93	99.78	99.68	99.26	100.25	99.29
Sum	99.70	99.70	99.95	99.85	99.67	99.92	99.62	99.65	100.15	Formula							
Formula										Fe	1.11	1.09	1.13	1.16	1.06	1.04	1.06
Fe	0.99	0.99	0.99	0.99	0.99	0.99	0.99	0.99	1.01	S	2.07	1.99	1.95	1.95	1.94	1.95	1.93
S	2.01	2.01	2.01	2.01	2.01	2.01	2.01	2.01	1.99	Cu	0.81	0.92	0.92	0.89	1.00	1.00	1.00
Sum	3.00	3.00	3.00	3.00	3.00	3.00	3.00	3.00	3.00	Sum	4.00	4.00	4.00	4.00	4.00	4.00	4.00
Ni–pyrrhotite				Ni–Co–Fe sulfarsenide						Sphalerite				Free gold			
Fe	58.93	58.37	58.29	10.93	10.67	10.72	8.04	9.74		Fe	5.88	4.20	4.52	6.96	Ag	7.41	5.36	6.33
S	37.77	38.22	37.88	24.82	24.72	24.32	23.56	23.88		S	32.56	33.30	34.25	32.65	Te	0.01	–	–
As	0.12	0.59	0.24	39.81	39.15	39.63	41.94	41.24		Cu	1.54	2.21	0.82	0.71	Au	92.26	94.26	92.74
Co	–	–	–	22.69	22.34	22.74	23.34	22.04		Zn	60.02	59.26	60.32	59.96	Sb	–	0.06	0.03
Ni	1.51	1.28	1.65	2.14	2.84	2.21	2.58	2.28		Ag	–	–	–	–	Sum	99.81	99.68	99.10
Au	0.08	0.06	0.10	0.08	0.09	0.07	0.08	0.09		Au	–	–	–	–	Formula			
Sum	98.41	98.52	98.16	100.46	99.80	99.70	99.54	99.28		Sb	–	–	–	–	Ag	0.13	0.09	0.11
Formula										Sum	100.02	99.02	99.91	100.30	Te	–	–	–
Fe	0.93	0.92	0.92	0.31	0.30	0.30	0.23	0.28		Formula					Au	0.87	0.91	0.89
S	1.04	1.05	1.05	1.21	1.21	1.19	1.17	1.19		Fe	0.10	0.07	0.08	0.12	Sb	–	–	–
As	–	0.01	–	0.83	0.82	0.83	0.89	0.88		S	0.98	1.01	1.02	0.98	Sum	1.00	1.00	1.00
Co	–	–	–	0.60	0.59	0.61	0.63	0.60		Cu	0.02	0.03	0.01	0.01				
Ni	0.02	0.02	0.02	0.06	0.08	0.06	0.07	0.06		Zn	0.89	0.88	0.89	0.89	Fineness	924.36	945.63	935.82
Sum	2.00	2.00	2.00	3.00	3.00	3.00	3.00	3.00		Sum	2.00	2.00	2.00	2.00				

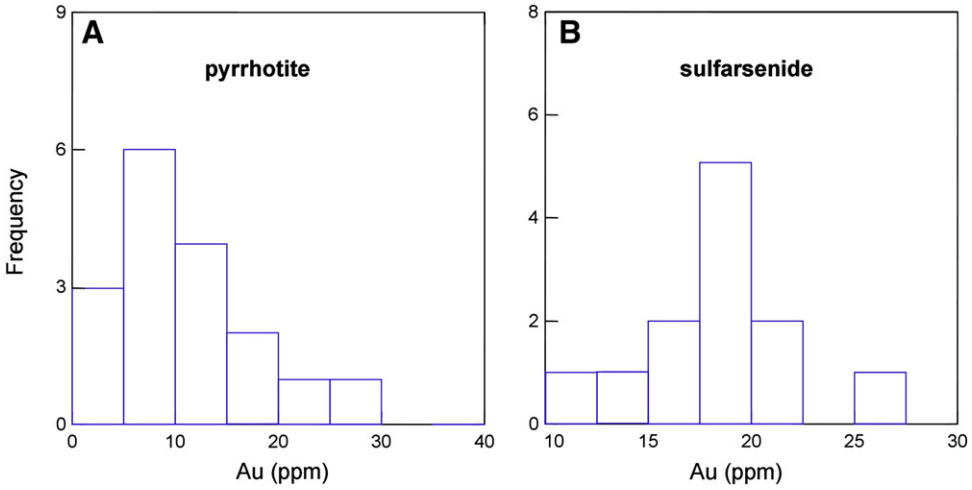

Fig. 5. Histogram of gold contents in pyrrhotite and sulfarsenide grains in the Um Eleiga Au deposit by LA-ICP MS.

0.6 to −0.1‰, with a mean value of 0.2‰. Measurements on sphalerite separates yield consistently negative $\delta^{34}S$ values (from −0.4 to −0.1‰). Assuming that sulfur was predominant as H_2S in the ore fluids, $\delta^{34}S_{H2S}$ values 0.7 to −0.5‰, average 0‰ (Table 3; Fig. 6) may be taken as the bulk sulfur isotope composition of the hydrothermal fluids ($\delta^{34}S_{\sum S}$) using mineral-H_2S fractionation factors Czamanske and Rye [38] and Ohmoto and Rye [39] at 350–375 °C (chlorite geothermometry). Differences induced by calculation of the fluid ($\delta^{34}S_{\sum S}$) values at the highly variable chlorite temperatures are slight.

Carbon isotope measurements on 9 calcite separates from quartz–carbonate veins give $\delta^{13}C$ values of −3.1 to −1.8‰, with a mean value of −2.4‰ (Table 4). Using the calcite–CO_2 fractionation equation of Ohmoto and Rye [39], the fluid $\delta^{13}C_{CO2}$ values at 350 and 375 °C range between −0.6 and 0.6‰, and cluster around 0‰ (Table 4). The $\delta^{18}O$ values for calcite range between 10.3 and 13.0‰, and there is no covariance between the C and O isotope data (Table 4). If isotopic equilibrium was achieved between deposited calcite in the ore zones and an H_2O-dominated ore fluid, these values would indicate fluid $\delta^{18}O_{H2O}$ values between 6.5 and 9‰ for the temperature range 350 to 375 °C [40]. Oxygen fractionation factor of quartz–water [41] at these temperatures indicates that fluids from which vein quartz (with $\delta^{18}O = 11.7–14.3$‰) have $\delta^{18}O_{H2O}$ values of 6.8 to 9.4‰, which are tightly comparable with those calculated for vein calcite (Table 4).

Table 3
Sulfur isotope values of sulfides from Um Eleiga gold deposit.

Sample	Mineral	Measured $\delta^{34}S$ (VCDT)‰	Calculated fluid $\delta^{34}S_{H2S}$ (VCDT)‰
Elg_23	Py	1.4	0.4
Elg_51	Py	0.7	−0.2
Elg_33a	Py	0.5	−0.5
Elg_24	Py	1.2	0.2
Elg_29	Py	0.6	−0.4
Elg_16	Py	0.8	−0.2
Elg_34	Py	1.3	0.3
Elg_50a	Py	1.4	0.5
Elg_20	Py	1.5	0.5
Elg_12	Py	0.5	−0.5
Elg_50a	Ccp	0.4	0.5
Elg_33a	Ccp	0.2	0.3
Elg_11	Ccp	0.6	0.7
Elg_20	Ccp	−0.3	−0.2
Elg_24	Ccp	−0.1	0.0
Elg_24	Sp	−0.2	−0.3
Elg_33a	Sp	−0.4	−0.4
Elg_20	Sp	−0.1	−0.2

Calculations are based on fractionation equations of Czamanske and Rye [38] and Ohmoto and Rye [39] at average 362 °C. 1σ is estimated as 0.19‰ for pyrite (Py) and chalcopyrite (Ccp) and as 0.12‰ for sphalerite (Sp).

7. Discussion and conclusions

The Um Eleiga complex is a calc-alkaline rock suite ranging in composition from quartz gabbro, diorite, tonalite to subordinate granodiorite. Field relationships, petrographic and geochemical data suggest formation through in-situ fractional crystallization at relatively shallow levels in an island–arc environment. Takla et al. [42] suggested a genetic model of the Um Eleiga gold deposit, in which the ore fluids and metal circulation were concomitant with the emplacement of a late granitic intrusion into the host intrusion. However, distribution of the gold bearing lodes is confined to gabbro–diorite transition, and shows no spatial relationship with the late granite bodies, cutting the intrusion peripheries.

Zoheir et al. [19] indicate that the Um Eleiga complex has oxygen fugacity ($\log fO_2$ −12 to −15) close to the hematite/magnetite oxygen buffer, implying a strong association with highly oxidized I-type magnetite series granitoids typical for Cu–Au porphyries [43]. Assimilation plus circulation of hydrothermal systems during emplacement may transform an oxidized arc magma to relatively reduced I-type granite, i.e. ilmenite becomes the dominant Fe–Ti oxide in the granitoids. It is therefore, suggested that local redox controls on the Um Eleiga suite played an important role in gold mineralization [44].

Gold in fossil terraces along the central catchment in the study area is similar to the auriferous placers that are commonly derived from intrusion-related gold systems and have been an important historical lure to lode gold potential in many provinces [45]. Location within or adjacent to the source intrusion may argue for a proximal hydrothermal deposit according to the classification scheme of Hart et al. [46]. Erosion of large areas of felsic portions of the Um Eleiga complex containing small but widespread gold lodes most likely provided the large amount of alluvial gold in the drainage developed in and around the gabbro–diorite gradational transition. Much of this

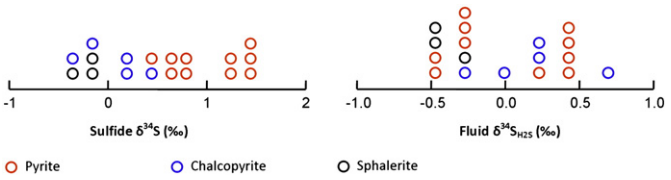

Fig. 6. Measured $\delta^{34}S$ and calculated fluid $\delta^{34}S_{H2S}$ values of sulfide minerals of the Um Eleiga gold deposit. (See text for details on the used fractionation equations).

Table 4
Carbon and oxygen isotope values of calcite and quartz in lodes from Um Eleiga gold deposit.

Sample	Mineral	$\delta^{13}C$ (PDB)‰	$\delta^{18}O$ (VSMOW)‰	[a]Fluid $\delta^{13}C$ CO_2‰	[b]Fluid $\delta^{18}O$ H_2O‰
Elg_24	Cal	−2.9	11.0	−0.4	6.7
Elg_33a	Cal	−2.6	11.9	−0.1	7.9
Elg_51	Cal	−2.1	10.7	0.4	6.8
Elg_34	Cal	−1.9	10.3	0.6	6.3
Elg_16	Cal	−2.6	12.1	−0.1	8.2
Elg_29	Cal	−2.7	11.1	−0.2	7.1
Elg_50a	Cal	−1.8	13.0	0.7	9.0
Elg_11	Cal	−2.0	11.3	0.5	7.3
Elg_23	Cal	−3.1	10.7	−0.6	6.8
Elg_24	Qtz		12.3		7.4
Elg_29	Qtz		13.3		8.4
Elg_50a	Qtz		12.1		7.2
Elg_33a	Qtz		11.7		6.8
Elg_51	Qtz		13.2		8.3
Elg_34	Qtz		12.4		7.5
Elg_16	Qtz		14.3		9.4
Elg_29	Qtz		12.7		7.8
Elg_12	Qtz		11.8		6.9
Elg_20	Qtz		12.8		7.9

[a] CO_2-calcite equation of Ohmoto and Rye [39],
[b] Calcite–water fractionation equation of O'Neil et al. [40], and quartz–water equation of Matsuhisa et al. [41] at average 365 °C. Total analytical errors of $\delta^{13}C$ and $\delta^{18}O$ of calcite (Cal) and quartz (Qtz) were within ±0.2‰ (1σ).

gold occurs in quartz vein fragments. Block faulting and westward tilting due paleotopography, as well as significant capture-initiated drainage changes likely resulted in varying deposition, preservation and reworking of the alluvial materials.

Electron microprobe data of the hydrothermal gangue phases, i.e., chlorite, sericite and calcite show homogeneity in composition of each indicating a kind of equilibrium between the hydrothermal fluids and host rocks. LA-ICP-MS results showed invisible gold in Ni–pyrrhotite and Ni–Co–Fe sulfarsenide phases disseminated in the quartz lodes. The occurrence of Co–Ni sulfarsenide in basic and ultrabasic rocks is generally considered to be of hydrothermal origin [47]. According to the hydrothermal hypothesis, cobaltite–gersdorffite could represent original magmatic Fe–Ni-sulfides that have been modified by a As–Co-rich fluid penetrating along the cleavage planes of the phenocrysts, and probably responsible for the very subordinate secondary assemblage [48]. On the other hand, late pyrite contains small inclusions of visible gold and is associated with dispersed gold blebs. Chalcopyrite and sphalerite contain no visible or dissolved gold. The high fineness, free-milling gold inclusions in pyrite and along microfractures may have been remobilized from dissolved gold in high-temperature mono-sulfide and sulfarsenide phases through infiltration of the hydrothermal fluids into fractured gabbro–diorite rocks. Similarly, Wagner et al. [49] suggest that gold is progressively liberated from massive sulfide ores during metamorphism and reprecipitated in veins and other low-strain sites.

Assuming depositional temperatures from 350 °C to 375 °C, based on chlorite geo-thermometry constraints, the $\delta^{34}S$ values of H_2S in ore fluids 0.7 to −0.5‰, with an average of 0‰. The minor variability of the results suggests a uniform sulfur source, while the near zero S^{34} values are generally considered to indicate a magmatic source. Similarly, the calculated fluid $\delta^{13}C_{CO2}$ values (−0.6 to 0.6‰, for the temperature range 350–375 °C of associated hydrothermal chlorite) cluster around 0‰, consistent with a magmatic source for carbon. Oxygen isotope data for vein quartz and calcite from the oreshoots indicate fluid $\delta^{18}O$ values of between 6.2 and 9.6‰, close to magmatic water, which according to Taylor [50] varies between 7.5 and 9.0, thus, supporting a magmatic origin of the hydrothermal 'metasomatic' fluid.

Acknowledgments

The author expresses his deep thanks to Profs. B. Lehmann (TU-Clausthal), R. Goldfarb (USGS) and R. Moritz (Univ. Geneva, Switzerland) for permitting accessibility to the different analytical facilities. Prof. J. Sneddon, the journal Editor is thanked for his inspiring comments on the manuscript.

References

[1] M.F. El-Ramly, S.S. Ivaanov, G.C. Kochin, The occurrence of gold in the Eastern Desert of Egypt. Studies on some mineral deposits of Egypt. Part I, Sec. A, Metallic Minerals, Geol. Surv. Egypt (1970) 53–63.
[2] A.M. Sabet, V.P. Bondonosov, The gold ore formations in the Eastern Desert of Egypt, Ann. Geol. Surv. Egypt 14 (1984) 35–42.
[3] Sh.Z. Gabra, Gold in Egypt: a commodity package, Geological Survey of Egypt, 1986.
[4] A.A. Hussein, Mineral deposits, in: R. Said (Ed.), The Geology of Egypt, Balkema, Rotterdam, 1990, pp. 511–566.
[5] N.Sh. Botros, A new classification of the gold deposits of Egypt, Ore Geol. Rev. 25 (2004) 1–37.
[6] M.M. Hassaan, K.E. El-Sawy, Tectonic environments and distribution of gold deposits in the Pan African Nubian Shield, Egypt, Aust. J. Basic Appl. Sci. 3 (2) (2009) 797–809.
[7] J. Naden, M.T. Styles, P.J. Henney, Characterisation of gold from Zimbabwe: part 1. bedrock gold, British Geological Survey Technical Report WC/94/51, 1994, 88 pp.
[8] R.C. Leake, R.J. Chapman, D.J. Bland, E. Condiffe, M.T. Styles, Microchemical characterization of gold from Scotland, Trans. Inst. Min. Metall. B Appl. Earth Sci. 106 (1997) 85–98.
[9] M. Potter, M.T. Styles, Gold characterization as a guide to bedrock sources for the Estero Hondo alluvial gold mine, western Ecuador, Appl. Earth Sci. (Trans. Inst. Min. Metall. B) 112 (2003) 297–304.
[10] F. Robert, R. Brommecker, B.T. Bourne, P.J. Dobak, C.J. McEwan, R.R. Rowe, X. Zhou, Models and exploration methods for major gold deposit types, in: B. Milkereit (Ed.), Proceedings of Exploration 07: 5th Decennial International Conference on Mineral Exploration, 2007, pp. 691–711.
[11] R.W. Boyle, The geochemistry of gold and its deposits, Geol. Surv. Can. Bull. (1979) 280–583.
[12] S.J. Barnes, W.D. Maier, The fractionation of Ni, Cu and the noble metals in silicate and sulfide liquids, in: R.R. Keays, C.M. Lesher, P.C. Lightfoot, C.E.G. Farrow (Eds.), Dynamic processes in magmatic ore deposits and their application in mineral exploration, Geological Association of Canada, Short Course, 13, 1999, pp. 69–106.
[13] P.A. Candela, A review of shallow, ore-related granites: textures, volatiles, and ore metals, J. Petrol. 38 (1997) 1619–1633.
[14] P.J. Jugo, P.A. Candela, P.M. Piccoli, Magmatic sulfides and Au:Cu ratios in porphyry deposits: an experimental study of copper and gold partitioning at 850 °C, 100 MPa in a haplogranitic melt–pyrrhotite–intermediate solid solution–gold metal assemblage, at gas saturation, Lithos 46 (1999) 573–589.
[15] G. Simon, S.E. Kesler, E.J. Essene, Gold in porphyry copper deposits: experimental determination of the distribution of gold in the Cu–Fe–S system at 400° to 700 °C, Econ. Geol. 95 (2000) 259–270.
[16] W.E. Halter, C.A. Heinrich, T. Pettke, Magma evolution and formation of porphyry Cu–Au ore fluids: evidence from silicate and sulfide melt inclusions, Miner. Deposita 39 (2005) 845–863.
[17] L.M. Cathles, Fluid flow and genesis of hydrothermal ore deposits, Economic Geology, 75th Anniversary Volume, 1981, pp. 424–457.
[18] W.J. Davis, G. Chi, S. Castonguay, M. McLeod, Temporal relationships between plutonism, metamorphism, and gold mineralization in southwestern New Brunswick: U–Pb and 40Ar/39Ar geochronological constraints, Curr. Res. Geol. Surv. Can. F2 (2004) 1–20.
[19] B.A. Zoheir, A.M. Mehanna, N.N. Qaoud, Geochemistry and geothermobarometry of the Um Eleiga Neoproterozoic island arc intrusive complex, SE Egypt: genesis of a potential gold-hosting intrusion, Appl. Earth Sci. (Trans. Inst. Min. Metall. B) 117 (3) (2008) 89–111.
[20] A. Kröner, R. Greiling, T. Reischmann, I.M. Hussein, R. Stern, S. Durr, J. Kruger, M. Zimmer, Pan-African crustal evolution in northeast Africa, in: A. Kröner (Ed.), Proterozoic lithosphere evolution, American Geophysical Union, Geod. Series, 17, 1987, pp. 235–257.
[21] R.J. Stern, Arc assembly and continental collision in the Neoproterozoic East African Orogen: implications for the consolidation of Gondwanaland, Annu. Rev. Earth Planet. Sci. 22 (1994) 319–351.
[22] A.M. Abdel-Rahman, Tectonic–magmatic stages of shield evolution: the Pan-African belt in northeastern Egypt, Tectonophysics 242 (1995) 223–240.
[23] A.M. Abdel-Rahman, Petrogenesis of early-orogenic diorites, tonalites and post-orogenic trondhjemites in the Nubian Shield, J. Petrol. 31 (6) (1990) 1285–1312.
[24] S. El-Gaby, F.K. List, R. Tehrani, The basement complex of the Eastern Desert and Sinai, in: R. Said (Ed.), The Geology of Egypt, Brookfield, Balkema, Rotterdam, 1990, pp. 175–184.
[25] A.H. Hashad, Present status of geochronological data on the Egyptian basement complex, Inst. Geol. (Jeddah) 4 (1980) 31–46.
[26] A.M. Abdel-Rahman, R. Doig, The Rb–Sr geochronological evolution of the Ras Gharib segment of the northern Nubian Shield, J. Geol. Soc. London 144 (1987) 577–586.

[27] M.L. Abdel-Khalek, M.A. Takla, A. Sehim, Z. Hamimi, A.W. El Manawi, Geology and tectonic evolution of Wadi Beitan area, South Eastern Desert, Egypt, Geology of the Arab World, 1, Cairo University, Cairo, 1992, pp. 369–394.
[28] D.D. Klemm, R. Klemm, A. Murr, Gold of the Pharaohs-6000 years of gold mining in Egypt and Nubia, J. Afr. Earth Sci. 33 (2001) 643–659.
[29] O.A. Hassan, M.M. El-Manakhly, Gold deposits in the southern Eastern Desert, Egypt, A Commodity Package, Egyptian Geological Survey and Mining Authority, Cairo, 1986.
[30] J.T. Armstrong, CITZAF: a package of correction programs for the quantitative electron microbeam X-ray analysis of thick polished materials, thin films, and particles, Microbeam Anal. 4 (1995) 177–200.
[31] E. Van Achterbergh, C.G. Ryan, S.E. Jackson, W.L. Griffin, LA-ICP-MS in the Earth Sciences — appendix 3, data reduction software for LA-ICP-MS, in: P.J. Sylvester (Ed.), Short Course, volume 29, Mineralogical Association of Canada, St. John's, 2001, pp. 239–243.
[32] M. Cathelineau, Cation site occupancy in chlorites and illites as a function of temperature, Clay Miner. 23 (1988) 471–485.
[33] E.C. Jowett, Fitting iron and magnesium into the hydrothermal chlorite geothermometer: GAC/MAC/SEG Joint Annual Meeting (Toronto, May 27–29, 1991), Program with Abstracts, 16, 1991, p. A62.
[34] D.D. Klemm, Synthesen und Analysen in den Dreiecksdiagrammen FeAsS–CoAsS–NiAsS und FeS2–CoS2–NiS2, Neues Jahrb. Mineral. Abh. 103 (1965) 205–255.
[35] S.R. Hem, E. Makovicky, The system Fe–Co–Ni–As–S. II. Phase relations in the (Fe, Co, Ni)As1.5S0.5 section at 650 and 500 °C, Can. Mineral. 42 (2004) 63–86.
[36] G.L. Cygan, P.A. Candela, Preliminary study of gold partitioning among pyrrhotite, pyrite, magnetite, and chalcopyrite in gold-saturated chloride solutions at 600 to 700 °C, 140 MPa (1400 bars), in: J.F.H. Thompson (Ed.), Magmas, Fluid, and Ore Deposits, Short Course Series, Mineral. Assoc. Canada, Ontario, 23, 1995, pp. 129–137.
[37] J.M. McCrea, On the isotopic chemistry of carbonates and a paleotemperature scale, J. Chem. Phys. 18 (1950) 849–857.
[38] G.K. Czamanske, R.O. Rye, Experimentally determined sulfur isotope fractionation between sphalerite and galena in the temperature range 600 to 275 °C, Econ. Geol. 69 (1974) 17–25.
[39] H. Ohmoto, R.O. Rye, Isotopes of sulfur and carbon, in: H.L. Barnes (Ed.), Geochemistry of Hydrothermal Ore Deposits, Second Edition, John Wiley & Sons, 1979, pp. 509–567.
[40] J.R. O'Neil, R.N. Clayton, T.K. Mayeda, Oxygen isotope fractionation in divalent metal carbonates, J. Chem. Phys. 51 (1969) 5547–5558.
[41] Y. Matsuhisa, J.R. Goldsmith, R.N. Clayton, Oxygen isotope fractionation in the system quartz–albite–anorthite–water, Geochim. Cosmochim. Acta 43 (1979) 113–140.
[42] M.A. Takla, A.A. El-Dougdoug, A.H. Rasmay, A.A. Gad, H.K. El-Tabbal, Origin of Um Eleiga gold mineralization, south Eastern Desert, Egypt, Egypt J. Mineral. 2 (1990) 3–20.
[43] J.R. Lang, T. Baker, Intrusion-related gold systems: the present level of understanding, Miner. Deposita 36 (2001) 477–489.
[44] S. Ishihara, Granitoid series and mineralization in the Circum-Pacific Phanerozoic Granitic Belts, Resour. Geol. 48 (1988) 219–224.
[45] R.J. Goldfarb, C.J.R. Hart, M.L. Miller, L.D. Miller, G.L. Farmer, D.I. Groves, The Tintina Gold Belt—A Global Perspective, British Columbia and Yukon Chamber of Mines, Cordilleran Roundup, 2000, pp. 5–34.
[46] C.J.R. Hart, T. Baker, M. Burke, New Exploration Concepts for Country-rock-hosted, Intrusion-related Gold Systems: Tintina Gold Belt in Yukon, British Columbia and Yukon Chamber of Mines, Cordilleran Roundup, 2000, pp. 145–172.
[47] M. Leblanc, Co–Ni arsenide deposits with accessory gold, in ultramafic rocks from Morocco, Can. J. Earth Sci. 23 (1986) 1592–1602.
[48] D. Béziat, P. Monchoux, F. Tollon, Cobaltite–gersdorffite solid solution as a primary magmatic phase in spessartite, Lacaune area, Montagne Noire, France, Can. Mineral. 34 (1996) 503–512.
[49] T. Wagner, R. Klemd, T. Wenzel, B. MAttsson, Gold upgrading in metamorphosed massive sulfide ore deposits: direct evidence from laser-ablation-inductively coupled plasma-mass spectrometry analysis of invisible gold, Geology 35 (2007) 775–778.
[50] J. Taylor, J. Frechen, E. Degens, Oxygen and carbon isotope studies of carbonatites from the Laaeher See District West Germany and the Alno District, Sweden, Geochim. Cosmochim. Acta (1967) 31.